AD-A024 148

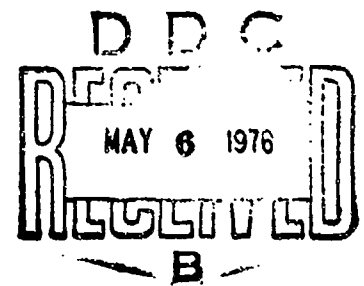# DIRECTIONAL SLOPE AND CURVATURE DISTRIBUTIONS OF WIND WAVES

HYDRONAUTICS, INCORPORATED

PREPARED FOR

OFFICE OF NAVAL RESEARCH

JANUARY 1975

134100

AD A024148

This document has been approved for public
release and sale; its distribution is unlimited.

The views and conclusions contained in this document
are those of the authors and should not be interpreted
as necessarily representing the official policies,
either expressed or implied, of the Advanced Research
Projects Agency or the U. S. Government.

HYDRONAUTICS, incorporated
research in hydrodynamics

HYDRONAUTICS, Incorporated

Technical Report 7211-7

Directional Slope and
Curvature Distributions
of Wind Waves

by

Jin Wu

January 1975

This document has been approved for public
release and sale; its distribution is unlimited.

The views and conclusions contained in this document
are those of the authors and should not be interpreted
as necessarily representing the official policies,
either expressed or implied, of the Advanced Research
Projects Agency or the U. S. Government.

ACCESSION for

NTIS   W. Ir Section ☑
DDC   E . A .al ☐
UNA...   ☐
JUSTI... .

BY
DISTRIBUTION/AVAILABILITY CODES

Dist.   A .t. a   or SPECIAL

A

REPORT DOCUMENTATION PAGE		READ INSTRUCTIONS BEFORE COMPLETING FORM
1. REPORT NUMBER Technical Report 7211-7	2. GOVT ACCESSION NO.	3. RECIPIENT'S CATALOG NUMBER
4. TITLE (and Subtitle) DIRECTIONAL SLOPE AND CURVATURE DISTRIBUTIONS OF WIND WAVES		5. TYPE OF REPORT & PERIOD COVERED Technical Report
		6. PERFORMING ORG. REPORT NUMBER T.R. 7211-7
7. AUTHOR(s) Jin Wu		8. CONTRACT OR GRANT NUMBER(s) N00014-72-C-0509
9. PERFORMING ORGANIZATION NAME AND ADDRESS HYDRONAUTICS, Incorporated 7210 Pindell School Road, Howard Co., Laurel, Maryland 20810		10. PROGRAM ELEMENT, PROJECT, TASK AREA & WORK UNIT NUMBERS NR 062-472
11. CONTROLLING OFFICE NAME AND ADDRESS Advanced Research Projects Agency Arlington, Virginia 22209		12. REPORT DATE January 1975
		13. NUMBER OF PAGES 40
14. MONITORING AGENCY NAME & ADDRESS(If different from Controlling Office) Office of Naval Research Department of the Navy Arlington, Virginia 22209		15. SECURITY CLASS. (of this report) Unclassified
		15a. DECLASSIFICATION/DOWNGRADING SCHEDULE None

16. DISTRIBUTION STATEMENT (of this Report)

This document has been approved for public release and sale; its distribution is unlimited.

17. DISTRIBUTION STATEMENT (of the abstract entered in Block 20, If different from Report)

18. SUPPLEMENTARY NOTES

19. KEY WORDS (Continue on reverse side if necessary and identify by block number)

Wind Waves   Wave-Wave Interaction
Roughness of the Sea Surface
Curvature Distributions of Wind Waves
Wind Wave Interaction

20. ABSTRACT (Continue on reverse side if necessary and identify by block number)

The slope and curvature distributions of wind waves along two principal axes (upwind-downwind and crosswind) have been measured in a laboratory tank under various wind velocities. In both directions, the slope distributions are very closely Gaussian, and the components of the mean-square water-surface slope vary logarithmically with the friction velocity of the wind. As the wind

20.   Cont'd.

velocity increases, the ratio between these two components in-
creases and falls between 0.5 and 0.6 at high wind velocities in
the gravity-governing regime of wind-wave interaction. The radius
of water-surface curvature, along either direction of measurement,
is found to be, generally, greater at a steeper viewing angle from
the normal to the mean water surface. The average radius of
curvature of the disturbed surface varies inversely with the
friction velocity of the wind. The ratio between the upwind-
downwind and crosswind components of the average radius of curva-
ture is unity at all wind velocities, indicating that the wind-
disturbed water surface is isotropic on the smallest scale. Other
results include that both the slope and curvature distributions
are askewed along the upwind-downwind direction, because of either
the presence of parasitic capillaries or the occurrence of wave
breaking.

HYDRONAUTICS, Incorporated

TABLE OF CONTENTS

HYDRONAUTICS, Incorporated

LIST OF FIGURES

HYDRONAUTICS, Incorporated

ABSTRACT

The slope and curvature distributions of wind waves along two principal axes (upwind-downwind and crosswind) have been measured in a laboratory tank under various wind velocities. In both directions, the slope distributions are very closely Gaussian, and the components of the mean-square water-surface slope vary logarithmically with the friction velocity of the wind. As the wind velocity increases, the ratio between these two components increases and falls between 0.5 and 0.6 at high wind velocities in the gravity-governing regime of wind-wave interaction. The radius of water-surface curvature, along either direction of measurement, is found to be, generally, greater at a steeper viewing angle from the normal to the mean water surface. The average radius of curvature of the disturbed surface varies inversely with the friction velocity of the wind. The ratio between the upwind-downwind and crosswind components of the average radius of curvature is unity at all wind velocities, indicating that the wind-disturbed water surface is isotropic on the smallest scale. Other results include that both the slope and curvature distributions are askewed along the upwind-downwind direction, because of either the presence of parasitic capillaries or the occurrence of wave breaking.

HYDRONAUTICS, Incorporated

1.   INTRODUCTION

The wind-disturbed water surface features ripples riding
on long waves.   There has been a great deal of interest in de-
termining, under various wind conditions, the statistical des-
criptions of the microstructure of the disturbed surface, the
pattern of ripples.   These wavelets have been considered
(Phillips 1966) to be involved in the inception of wind waves
as well as in the dissipation of wave energy.   In addition, the
microstructure has also been suggested to govern the reflection
and the backscattering of electro-magnetic waves (Newton and
Rouse 1972) impinging on, and radiation of thermal energy
(McGrath and Osborne 1973) from the air-sea interface.

Previous laboratory measurements (Schooley 1954, Cox 1958,
Wu 1971a) have sought to determine the upwind-downwind compo-
nents of mean-square slopes of the disturbed water surface under
various wind velocities.   Based on the friction velocity of the
wind, these laboratory-measured components alone were found (Wu
1971a) to be comparable with the total mean-square slopes mea-
sured in the field (Cox and Munk 1956).   A probable explanation
of this discrepancy was suggested earlier (Wu 1971a) as due to
the narrowness of the tank limiting the growth of crosswind
components.   The latter, however, have not been previously mea-
sured in the laboratory.   The distributions of upwind-downwind
curvatures of the disturbed water surface were also measured
(Wu 1972a), but, again, there have been no measurements of
crosswind components.

HYDRONAUTICS, Incorporated

In the present study, the distributions of upwind-downwind and crosswind slopes and curvatures of the disturbed surface were systematically measured under various wind velocities. The results, containing the first complete description of the microscopic structure of wind waves, are important for studying and modeling of the air-sea interface. In addition, the comparisons between the components measured along two principal axes, and between field and laboratory results, may provide some insight toward understanding energy transfer processes from wind to waves and among wave components.

2. WIND AND WAVE CONDITIONS

The experiments have been conducted in a wind-wave tank, which is 1.5 m wide and 22 m long. Mounted at the upwind end of the tank is an axial-flow fan, driven by a variable-speed motor; a permeable wave absorber is installed at the downwind end. The tank is covered for the first 15 m to provide an 0.31-m high wind tunnel above 1.24-m deep water channel. The maximum attainable wind velocity within the tunnel is 14 m/s. The test section is located at the middle length of the tank.

The wind boundary layer over the water surface has been surveyed with a pitot-static probe. As reported earlier (Wu 1968), the wind-velocity profiles in the tunnel follow the logarithmic law (Schlichting 1968) near, but not overly close to, the water surface (Figure 1), where u is the wind velocity measured above the mean water surface. The friction velocity (u_*) of the wind and the roughness length (z_0) of the wind boundary layer were determined from the wind-velocity profile:

HYDRONAUTICS, Incorporated

$$\frac{u}{u_*} = \frac{1}{\kappa} \ln\left(\frac{z}{\eta}\right) \quad , \quad \eta = \frac{z_0}{30} \qquad [1]$$

where κ is the Karman universal constant. The results are plotted in Figure 2, where U is the wind velocity measured at 2/3 of the tunnel height above the mean water surface. On the basis of the calculated friction velocity and roughness length, it was deduced that the wind boundary layer in the present tank became turbulent for U > 2.0 m/s and became aerodynamically rough for U > 2.5 m/s. Rhombic gravity wave cells were formed as soon as the wind boundary layer became turbulent. As the wind velocity increased beyond 3 m/s, parasitic capillaries were produced; this is the surface-tension governing regime of wind-wave interaction (Wu 1968). Wave breaking was observed at high wind velocities, U > 7 m/s, where gravity replaces surface tension as the governing parameter of wind-wave interaction.

From the wave profiles measured with a conductivity probe, the periods of more than 100 basic waves were obtained for each wind velocity. The average wavelength ($\overline{\lambda}$) was then calculated from the average period (P) and is plotted in Figure 3. It is noted that the wavelength was determined from the wave period with the influence of wind-induced drift currents (Wu 1973a, b) taken into account through iterations among the following expressions:

$$C_0 = \left(\frac{g\overline{\lambda}}{2\pi} + \frac{2\pi T}{\rho\lambda}\right)^{1/2} \quad ,$$

$$\alpha = (C_m - C_0)/V \quad , \text{ and}$$

$$f = \overline{\lambda}/C_m \qquad [2]$$

where C_o is the phase velocity according to the dispersion relationship, C_m is the measured phase velocity, g is the gravitational acceleration, T is the surface tension, ρ is the density of water, a is an experimentally determined coefficient, f is the frequency, and V is the surface drift current. The average wavelength calculated here corresponds to the length of the dominant wave; waves with their length longer than this length are not saturated, and waves with their length shorter than this length presumably fall into the equilibrium regime (Phillips 1966).

3. MEASUREMENTS OF MICROSTRUCTURE

3.1 Optical Instrument

The optical instrument consists principally of a light-source, a telescope, and photomultiplier unit (see Figure 4a). The instrument is supported on a carriage between two vertical circular-arch plates with their geometric centers at the mean water surface. The rectangular light sheet, produced by the light-source, and the axis of the telescope are within the same radial plane. The lenses of the light-box and of the telescope are focused on the mean water surface and at the center span of the vertical plates, or the center width of the tank. By means of sprockets and an endless chain, the carriage can be set anywhere along the arch to have the viewing angle of the optical instrument at any desired inclination from the mean water surface. With such arrangements, the photomultiplier receives reflected light only when the water surface is normal to the radial plane containing the light sheet and the telescopic axis.

The cross section of the light sheet is rectangular with a
large length-to-width ratio (20:1) and with its short side
aligned with the direction of measurement the observation plane
within which the instrument traverses. The calibrated slope
response of the optical instrument in this direction is shown
in Figure 4b. The angular tolerance of the instrument to the
water-surface slope in the direction of interest is seen to be
slightly greater than 1°; the tolerance in the transverse di-
rection is, therefore, about 20°.

As shown in Figure 4a, the two vertical plates, joined to-
gether by a base plate, is supported on top of a base ring. The
latter can be rotated to align the observation plane at any de-
sired angle with respect to the wind direction. Measurements
have been conducted in the present experiment along two principal
directions: Upwind-downwind and cross-wind.

The focal spot of the telescope on the water surface is
circular, 0.7-mm in diameter. This spot is completely bright
when the water surface is relatively flat and is partially bright
when the curvey water surface reflects part of the impinging
light away from the telescope (see Figure 4c). The width of the
bright portion, 2h , of the spot is related to the surface curv-
ature and the signal intensity is proportional to the ratio be-
tween the bright portion and the total area of the spot. The
curvature response of the instrument, relating signal to curva-
ture, can, therefore, be calculated geometrically and has been
calibrated with reflections from cylindrical surfaces of given
radii (Wu 1972a); the results are shown in Figure 4c. The

instrument has the same response for concave and convex surfaces
having the same magnitude . the radius of curvature. This is
achieved by adopting a s! ⊥ focal spot for the telescope and
by setting the instrument far enough from the water surface.

The light signal is continuous and saturated to a prescribed
level, insensitive to the change of surface curvature, as long
as the angular change of the wavy water surface from one face to
the other is less than the acceptance width of the instrume .:
(about 1°). As the angular change increases beyond that, or if
the surface curvature increases further, the signal becomes dis-
continuous. The signal then becomes essentially a light pulse.
The intensity of the signal, or the pulse height, is related to
the surface curvature; the period of the signal, or the pulse
width, is the time required for a detectable water-surface slope
to make its complete pass under the instrument.

3.2 Experimental Process and Data Acquisition

Two series of experiments have been conducted in the present
study to measure microstructures of the disturbed surface under
various wind velocities along both the upwind-downwind and the
crosswind directions. For each wind velocity, the optical ins-
trument was set successively at various angles of inclination
from the mean water surface, and data was taken over a constant
period of four minutes for each inclination. The signal pro-
duced by the reflecting water surface was fed continuously into
a pulse-height analyzer and was sorted automatically according
to its intensity into one of the 50 channels of the analyzer;
each channel has a preset intensity band, 1/50 of the saturation

voltage of the signal. The output of the analyzer, the intensity distribution of light pulses accumulated during a constant period of time for a given instrument inclination, was first traced on an x-y plotter and later digitized.

A set of sample data on the distribution of pulse height is shown in Figure 5a. The data are replotted in Figure 5b with the horizontal axis transformed from the channel number (or voltage) into the radius of curvature. The lower cutoff radius of curvature (L) of the present optical instrument is marked by a long vertical line shown on the left in Figure 5b. This cutoff, set well above the instrument noise, is about 5% of the saturation voltage of the signal and is about 1.7% of the maximum detectable radius of curvature. The upper cutoff (i.e., the maximum detectable) radius of curvature is 4 cm. A wavy surface with a radius of curvature beyond the upper cutoff would be registered as 4 cm, the cutoff value. Except at very low wind velocity, less than 2 m/s, the radius of curvature of the water surface seldom reaches the upper cutoff. The centroid is then determined of the area, shown in Figure 5b, enclosed by the measured distribution curve, the horizontal axis, and the lower cutoff radius of curvature. The calculated centroid ($\bar{r}$), indicated in the same figure, is the average absolute radius of curvature. Only the absolute value is measured here, because the present optical instrument, as discussed earlier, does not discriminate between concave and convex surfaces.

HYDRONAUTICS, Incorporated

4. RESULTS

4.1 Slope Distributions and Root-Mean-Square Slopes

As discussed in the previous section, the optical instrument is set successively, for each wind velocity, at various angles of inclination. A typical trace of signals automatically sorted and counted during a four-minute period for one instrument inclination was already shown in Figure 5a. From the digitized data, the total number of signals for one angle of observation can be obtained. Compiling the total number of signals from various angles accumulated for the constant period of time, we have the relative frequency of occurrence, of the distribution, of the water-surface slope. The distributions of upwind-downwind slopes under various wind velocities are plotted in Figure 6, where the negative sign indicates a windward slope and the positive sign indicates a leeward slope. The distributions of crosswind slopes under various wind velocities are shown in Figure 7.

For each wind velocity, the relative frequencies of occurrence of various water-surface slopes along both upwind-downwind and crosswind directions were found to follow very closely normal distributions. The data were first integrated to determine the mean slope, on either side of which the total frequency of occurrence of the water-surface slope is the same. This mean slope is called here the skewness of the slope distribution. On the basis of the calculated skewness, a Gaussian curve of one of the following forms is fitted to each set of data according to the least-square principles:

HYDRONAUTICS, Incorporated

-10-

$$f_\ell = \frac{1}{(2\pi\bar{\theta}_\ell)^{1/2}} \exp\left[-\frac{(\theta - \theta_{o\ell})^2}{2\bar{\theta}_\ell}\right]$$

or   [3]

$$f_c = \frac{1}{(2\pi\bar{\theta}_c)^{1/2}} \exp\left[-\frac{(\theta - \theta_{oc})^2}{2\bar{\theta}_c}\right]$$

where the subscripts ℓ and c are referred to the upwind-downwind
and the crosswind components, respectively; f is the frequency
of occurrence of the water-surface slope θ; $\bar{\theta}$ is the variance of
the data, or the root-mean-square water-surface slope; θ_o is the
skewness. The fitted curve is drawn as a continuous line to
each distribution shown in Figures 6 and 7.

The upwind-downwind and the crosswind components of the
mean-square surface slope, the square of the variance, are com-
piled in Figure 8. Both components of the mean-square surface
slope are seen to vary logarithmically with the friction veloc-
ity of the wind. Two straight lines are fitted on the basis of
the least-square principles to the data, excluding the data
point at the lowest wind velocity where the wind boundary layer
is not yet turbulent. The mean-square slopes along both the
upwind-downwind $(\overline{s_\ell^2})$ and the crosswind $(\overline{s_c^2})$ directions can be
expressed, respectively, as

$$\overline{s_\ell^2} = 0.0464\ \ell n(u_*) - 0.1127\ , \quad \overline{s_\ell^2} = (\tan\bar{\theta}_\ell)^2$$

[4]

$$\overline{s_\ell^2} = 0.0305\ \ell n(u_*) - 0.0903\ , \quad \overline{s_\ell^2} = (\tan\bar{\theta}_c)^2$$

HYDRONAUTICS, Incorporated

where u_* is expressed in cm/s. The total mean-square slope of
the disturbed surface, $\overline{s^2}$, is, therefore

$$\overline{s^2} = 0.0769 \; \ell n(u_*) - 0.203 \qquad\qquad [5]$$

4.2 Distributions and Averages of Radius of Curvature

The distributions of radii of curvature of the disturbed
surface along both upwind-downwind and crosswind directions were
obtained. The general shape of the distribution curve is shown
in Figure 5b. Because of the limitation on the lower cutoff of
detectable curvature of the instrument, a complete distribution
of radii of curvature, extending to very small radii, cannot be
obtained. The present measurement, however, are sufficient for
determining the average radius of curvature. Any uncertainty
on the lower end of the data, the right-hand side of Figure 5b,
would not affect the determination of the centroid of the area
under the distribution curve.

The average radii of curvature observed from various graz-
ing angles, calculated from the distribution curve such as that
shown in Figure 5b, are compiled in Figures 9 and 10; the
upwind-downwind components are shown in Figure 9, and the cross-
wind components in Figure 10. In both figures, the angular dis-
tribution of average radii of curvature is normalized with
respect to its frequency of occurrence, or the corresponding
slope distribution. The normalization only involves dividing
the observation angle by the variances of the slope distribu-
tion. Such a step, relating the average radius of curvature to

its relative frequency of occurrence, is helpful for comparing results obtained at various wind velocities with different slope distributions. The relative frequency of occurrence for the converted scale, on the basis of the standard deviation, is given by the Gaussian function, shown in Equation [3].

As shown in Figure 9, the average radius of curvature in the upwind-downwind direction is seen to have its minimum value at a small but positive viewing angle. The average radius generally increases when the observation changes continuously from zero to a negative viewing angle. For positive viewing angles, the average radius of curvature first decreases to the minimum value, and then increases when the observation angle increases. In general, the distribution of the average radii of curvature is symmetrical in the crosswind direction, and a large radius of curvature is obtained at a steep observation angle.

Each data point shown in Figures 9 and 10 is the average radius of curvature measured from a given viewing angle. The overall average radius of curvature for each wind velocity can, therefore, be obtained from the grouped data points and their corresponding frequencies of occurrence. The sum of the products between data points and their corresponding frequencies of occurrence was first determined, and then this sum was divided by the total frequency of occurrence to obtain the overall average radius of curvature. The results obtained from various wind velocities and along both upwind-downwind and crosswind directions are presented in Figure 11.

HYDRONAUTICS, Incorporated

As the friction velocity of the wind increases, the overall average radius of curvature of the disturbed water surface decreases. There appears to be no systematic deviation between the upwind-downwind and the crosswind components. At high wind-friction velocities with the carrier waves covered by ripples, the disturbed surface in the present tank is similar to the air-sea interface. The overall average radius of curvature, in this case, is seen in Figure 11 to vary with 2/3 power of the wind-friction velocity. The straight line shown in the figure corresponds to

$$\bar{r} = 42(u_*)^{-2/3} \hspace{3cm} [6]$$

where u_* is again expressed in cm/s.

5. DISCUSSION

5.1 Symmetry of Slope and Curvature Distributions

The skewnesses of the slope distributions, shown in Figures 6 and 7 and discussed earlier, are compiled in Figure 12a. For each curvature distribution shown in Figures 9 and 10, the first moment of the radius of curvature, with respect to the zero slope and weighted according to the frequency of occurrence, was calculated. This moment, indicating the skewness of the distribution of radius of curvature, is compiled in Figure 12b.

The distributions of slopes and curvatures in the crosswind direction, shown in Figures 7 and 10, are symmetrical about the zero slope, as no directionality of wave propagation is involved

HYDRONAUTICS, Incorporated

here. The skewnesses of these distributions in the crosswind
direction are seen in Figures 12a and 12b to be nearly zero.
Both distributions, however, are skewed in the upwind-downwind
direction, especially at low-wind velocities. The latter velocity
range falls into the regime where surface tension governs wind-
wave interaction. As reported earlier (Wu 1971a), the skewness
in this regime is due to the presence of parasitic capillaries
on the leeward face of the carrier-wave profile. The skewness
corresponds essentially to the slope of the leeward face of
carrier waves. The slight skewness of the slope distribution
observed at high wind velocities in the gravity-governing regime
of wind-wave interaction is believed (Wu 1971b) to be due to the
fact that wave breaking occurs near the crest but on the leeward
face of the carrier waves. Very violent wave breaking was ob-
served near the crest of every dominant wave at two of the high-
est wind velocities. The diminishing skewness seen at these two
wind velocities in Figures 12a and 12b may be explained as
three-dimensional roughnesses, or bubbling water surface accom-
panying wave breaking, which escape the present optical counting
technique but not the earlier glitter photography (Wu 1971b).
It is noted that such a skewed distribution may cause different
backscattering of electro-magnetic waves from the leeward and
the windward faces of carrier waves.

5.2 Isotropy of Microstructure of Wind-Disturbed Surface

The ratio between the upwind-downwind and the crosswind
components of the mean-square slope is presented in Figure 13a.
This ratio is seen in the figure to increase with the wind

velocity first rapidly and then gradually. At very low-wind velocities, the parasitic capillaries are the major contributors of the mean-square slope. These capillaries are long crested and propagate, generally, along the wind direction; therefore, the crosswind slope, in this case, is very small. As the wind velocity increases, resonant waves are produced. These resonant waves, longer ones of which carry parasitic capillaries, generally, propagate at large angles from the wind direction. Consequently, the crosswind slope becomes relatively more important. At high wind velocities in the gravity-governing regime of wind-wave interaction, the carrier waves are almost unidirectional, but their profiles are well covered by random short waves. In this case, the ratio between the crosswind and the upwind-downwind slopes varies only slightly with the wind velocity and is seen in Figure 13a to approach asymptotically a value nearly as high as 3/5.

The ratio between the crosswind and the upwind-downwind components of the overall average radius of curvature is shown Figure 13b. Although there is some scattering of the data, it is clear that this ratio has a value of unity for all wind velocities in both regimes of wind-wave interaction.

The carrier waves in the present tank are definitely directional, propagating predominantly along the direction of the wind. Described by the wave-height statistics, the carrier waves, however, have only secondary effects on the root-mean-square slope of the disturbed surface. The latter, the first derivative of wave height, is dominated by the ripples.

Consequently, despite the fact that the carrier waves are essentially unidirectional at high wind velocities, the slope statistics are much more isotropic than the height statistics. The statistics of surface curvature is seen in Figure 13b to be exactly isotropic, because the curvature statistics, the second derivative of wave height, are dominated by the smallest waves. In summary, the present results indicate that the microscopic structure of wind waves is isotropic.

Cox and Munk (1956) deduced slopes of the sea surface from the brightness distribution of photographs of sun glitter on the sea surface. The ratio between the crosswind and the upwind-downwind components of the mean-square sea-surface slope is plotted in Figure 14a, where U_{10} is the wind velocity measured at 10 meters above the mean-sea level (Wu 1972b). Comparing with Figure 13a, these ratios obtained from oceanic data are similar to those determined from laboratory results obtained at high wind velocities in the gravity governing regime of wind-wave interaction. This is understandable, as the surface-tension governing regime existing in laboratory tanks at low-wind velocities never exists in the field (Wu 1970, 1972c). Wind-wave interactions on oceanic scales fall into the gravity-governing regime for all wind velocities. The overall average ratio between the two components of the mean-square sea-surface slope is seen in Figure 14a to be about 3/4, indicating only an approximate isotropic spreading of high-frequency waves. Limited by the width of the tank, the value of the same ratio, measured in the laboratory, is only about 3/5. However, the difference may

be small enough to permit reasonably accurate modeling of the microstructure of the sea surface in the present facility.

5.3 Saturation of High Frequency Waves

The mean-square surface slopes measured at two different fetches in the present tank are compared in Figure 8. The values obtained earlier at a shorter fetch (11 m) is seen to be smaller than that obtained presently at a longer fetch (14 m). The mean-square slope of the wind disturbed water surface can be obtained from the directional wave number spectrum $\Psi(\bar{k})$, or

$$\overline{s^2} = \int_{k_0}^{k_\nu} k^2 \Psi(\bar{k}) d\bar{k} \qquad [7]$$

where k and $\bar{k}$ are wave-number scaler and vector, respectively; k_0 is the wave number at the spectral maximum; k_ν is the neutrally stable wave number. The latter corresponds to the wavelength at which the energy input from the wind is balanced by the energy dissipation through viscosity. The contribution from the wave number range $k < k_0$ to the mean-square slope is negligible, while the neutrally stable wave number serves as the upper cutoff.

The increase of the mean-square slope, observed in Figure 8 for the case of longer fetch, cannot be accounted for by the extension of the equilibrium wave spectrum at either low or high frequency end. Undoubtedly, the carrier waves grow in both length and height with fetch; however, their contribution to the mean-square surface slope as a result of this slight decrease

of k_o is negligible. The equilibrium portion of the spectrum
at the longer fetch cannot be expanded to higher frequencies
from that at the shorter fetch, because the friction velocity
of the wind at the longer fetch is even slightly smaller than
that at the shorter fetch (Wu 1973b). Taken together, the pres-
ent results appear to indicate an overall increase of energy
density over the entire spectrum. In other words, even the
high-frequency portion of the wave spectrum may not be truly
saturated in fetch-limited situations.

5.4 Comparison Between Laboratory and Field Results

Because of the great difference between wind fetches ex-
isting in the wind-wave tank and the field, the friction veloc-
ity rather than the wind velocity is used here as the basis
for comparison of slope data. Adopting a logarithmic wind
profile, the friction velocity·for Cox and Munk's data can be
calculated from either their own velocity measurements at two
different heights (12.5 and 2.75 m above the mean sea level)
or from the wind velocity measured at 12.5-m elevation and the
approximate wind-stress-coefficient (C_{10}) formula: $C_{10} = 0.5 \ U_{10}^{1/2}$
$\times 10^{-3}$. The friction velocities calculated by means of both
methods are about the same, but the results obtained with the
latter method are used, because the wind velocity measured at
the lower height (2.75 m) may be too close to the water surface
to be free from wave-induced motion, especially at high wind
velocities. The present results and the field data are plotted
versus the friction velocity of the wind in Figure 15.

The directional wave spectrum in the equilibrium range was proposed by Phillips (1966),

$$\text{Gravity range:} \quad \Psi(\bar{k}) = \frac{B}{\pi} k^{-4}$$

$$\text{Capillary range:} \quad \Psi(\bar{k}) = \frac{B'}{\pi} k^{-4}$$

[8]

where B and B' are the spectral coefficients for the gravity and the capillary ranges, respectively. These coefficients were considered originally to be constant and found recently to be fetch dependent. Substituting [8] into [7], we have

$$\overline{s^2} = B \, \ell n(k_\gamma/k_o) + B' \, \ell n(k_v/k_\gamma)$$

[9]

where k_γ is the wave number where the influence of surface tension on wave propagation is negligible. It has been shown (Wu 1972b) that oceanic slope data (Cox and Munk 1956) are divided into two groups as illustrated in Figure 14b. Gravity waves are the sole contributor to sea-surface slope at low wind velocities, with the right-hand side of [9] consisting only of the first term; both gravity and capillary waves contribute to sea-surface slope at high-wind velocities, with the right-hand side of [9] consisting of both terms. The portion of the oceanic data fitted by a straightline in Figure 15 is the second group. A straightline is also drawn to fit the laboratory data in Figure 15. It is interesting to see that the fitted line for the laboratory data with contributions from both gravity and capillary waves is parallel with the line fitted through the

HYDRONAUTICS, Incorporated

oceanic data with the same contributors. This fact appears to
indicate that the spectral coefficients B and B' have a much
larger value in the laboratory tank than in the field.

The results, that the mean-square slopes measured in the
laboratory with short dominant waves are much larger than
those measured in the field with long dominant waves, are con-
sistent with our earlier finding (Wu 1973c). With preexisting
long surface waves, the mean-square slope under identical wind-
friction velocity was found to be smaller than without. An
explanation was provided then that the long waves acting like
an energy sink prevent the growth of waves of intermediate
lengths. The latter contribute much more heavily to the mean-
square slope than the longer components.

6. CONCLUSIONS

The present results provide the first complete statistical
description of the microstructure of the wind-disturbed water
surface. The slope distributions of the surface are very
closely Gaussian along both upwind-downwind and the crosswind
directions. Both slope components are found to vary logarith-
mically with the friction velocity of the wind. Despite the
narrowness of the tank, the ratio between the crosswind and the
upwind-downwind mean-square slopes reaches as high as 3/5 in
the gravity governing regime of wind-wave interaction. The
ratio between the crosswind and the upwind-downwind components
of the average radius of curvature is unity at all wind veloc-
ities indicating that the microstructure of the surface is

always isotropic. The mean-square slope measured at the shorter fetch is greater than that obtained at the longer fetch suggesting that even the high-frequency portion of the wave spectrum is not truly saturated. The laboratory determined mean-square slope is found to be much larger than the oceanic value. This is believed to be due to the fact that the long waves absorb most of the energy supplied by the wind and prevent the growth of intermediate components.

HYDRONAUTICS, Incorporated

REFERENCES

Cox, C. S., and Munk, W. H., 1956, "Slopes of the Sea Surface Deduced from Photographs of Sun Glitter," 6, No. 9, Scripps Institution of Oceanography.

Cox, C. S., 1958, "Measurements of Slopes of High-Frequency Wind Waves," J. Mar. Res. 16, 199-225.

McGrath, J. R., and Osborne, M. F. M., 1973, "Some Problems Associated with Wind Drag and Infrared Images at Sea Surface," J. Phys. Oceangr. 3, 318-27.

Newton, R. W., and Rouse, J. W., Jr., 1972, "Experimental Measurements of 2.25-cm Backscatter from Sea Surfaces," IEEE Trans. GE-10, 2-7.

Phillips, O. M., 1966, "The Dynamics of the Upper Ocean," Cambridge University Press.

Schlichting, H., 1968, "Boundary-Layer Theory," 6th Ed. McGraw-Hill Book Company, New York.

Schooley, A. H., 1954, "A Simple Optical Method for Measuring the Statistical Distribution of Water Surface Slopes," J. Opt. Soc. Am., 44, 37-40.

Wu, Jin, 1968, "Laboratory Studies of Wind-Wave Interactions," J. Fluid Mech. 34, 91-112.

Wu, Jin, 1970, "Wind-Wave Interactions," Phys. Fluids 13, 1926-1930.

Wu, Jin, 1971a, "Slope and Curvature Distributions of Wind-Disturbed Water Surface," J. Opt. Soc. Am. 61, 852-58.

Wu, Jin, 1971b, "Observations on Long Waves Sweeping Through Short Waves," Tellus 23, 364-70.

Wu, Jin, 1972a, "Surface Curvature of Wind Waves Observed From Different Angles," J. Opt. Soc. Am. 62, 395-400.

Wu, Jin, 1972b, "Sea-Surface Slope and Equilibrium Wind-Wave
    Spectra," Phys. Fluids 15, 741-47.

Wu, Jin, 1972c, "Physical and Dynamical Scales for Generation
    of Wind Waves," J. Waterways, Harbor Coastal Engr. Div.
    ASCE 98, WW2, 163-75.

Wu, Jin, 1973a, "Effects of Wind-Induced Drift Currents on the
    Propagation of Surface Waves," HYDRONAUTICS, Incorporated
    Technical Report 7211-3.

Wu, Jin, 1973b, "Wind-Induced Drift Current," HYDRONAUTICS,
    Incorporated Technical Report 7303-3.

Wu, Jin, 1973c, "Rates of Growth and Decay of Wind Waves Under
    Conditions of Unsteady Wind," HYDRONAUTICS, Incorporated
    Technical Report 7211-4.
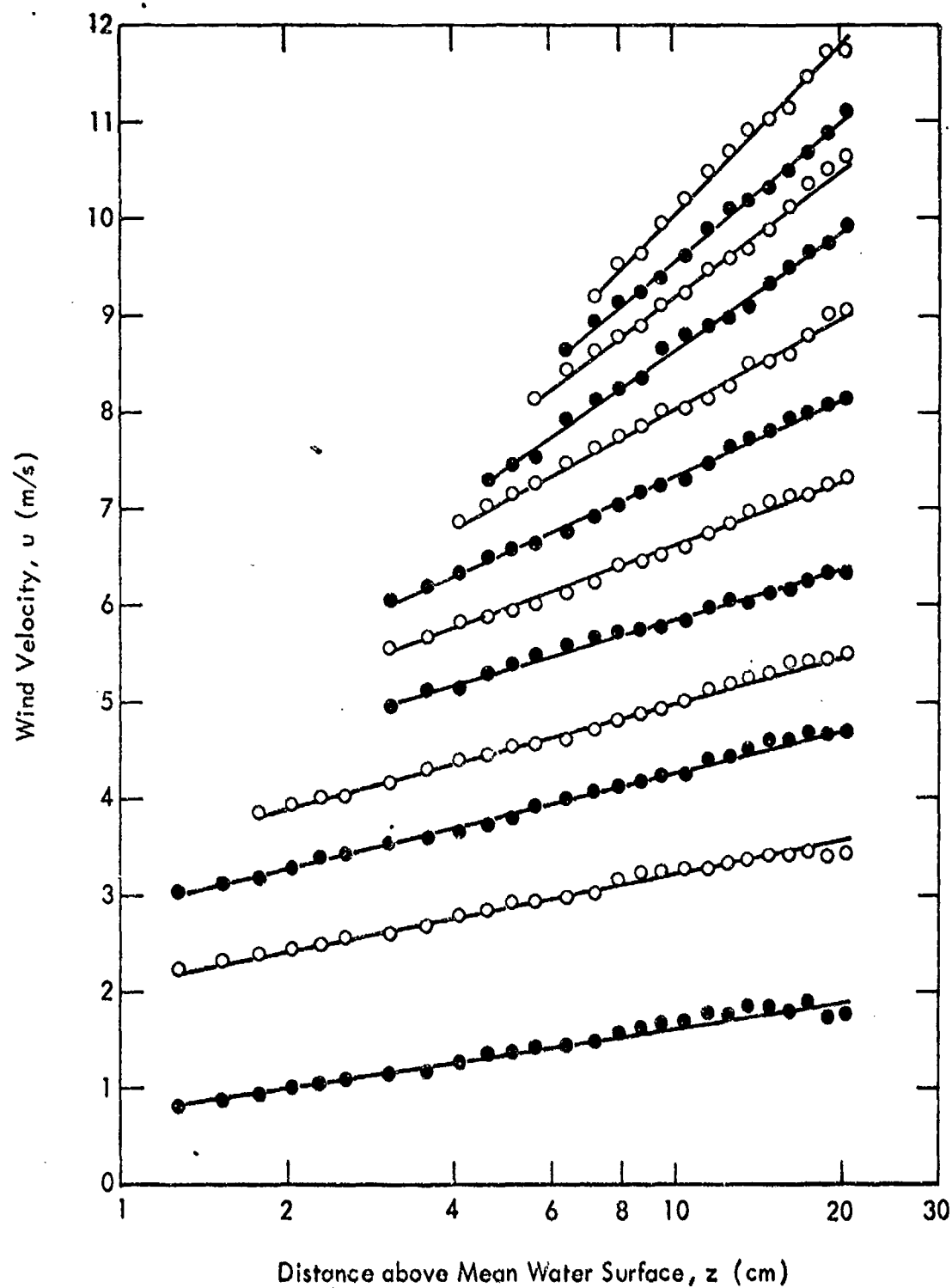
FIGURE 1 - DISTRIBUTIONS OF WIND VELOCITIES. The profiles from bottom to top were obtained at the order of increasing free-stream wind velocities. The straight lines are fitted according to the least-square principle.
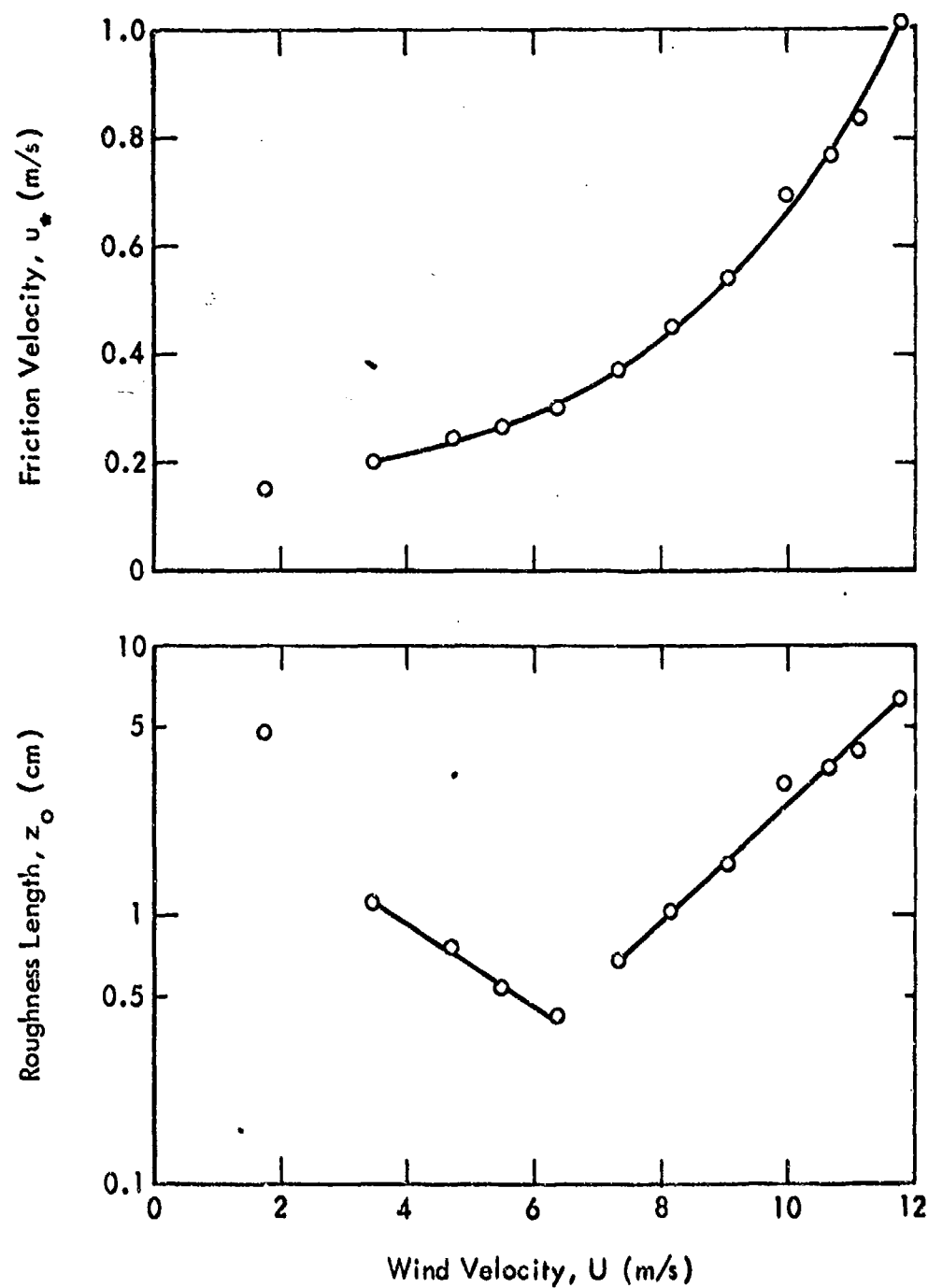
FIGURE 2 - FRICTION VELOCITY OF WIND AND ROUGHNESS
LENGTH OF WIND BOUNDARY LAYER
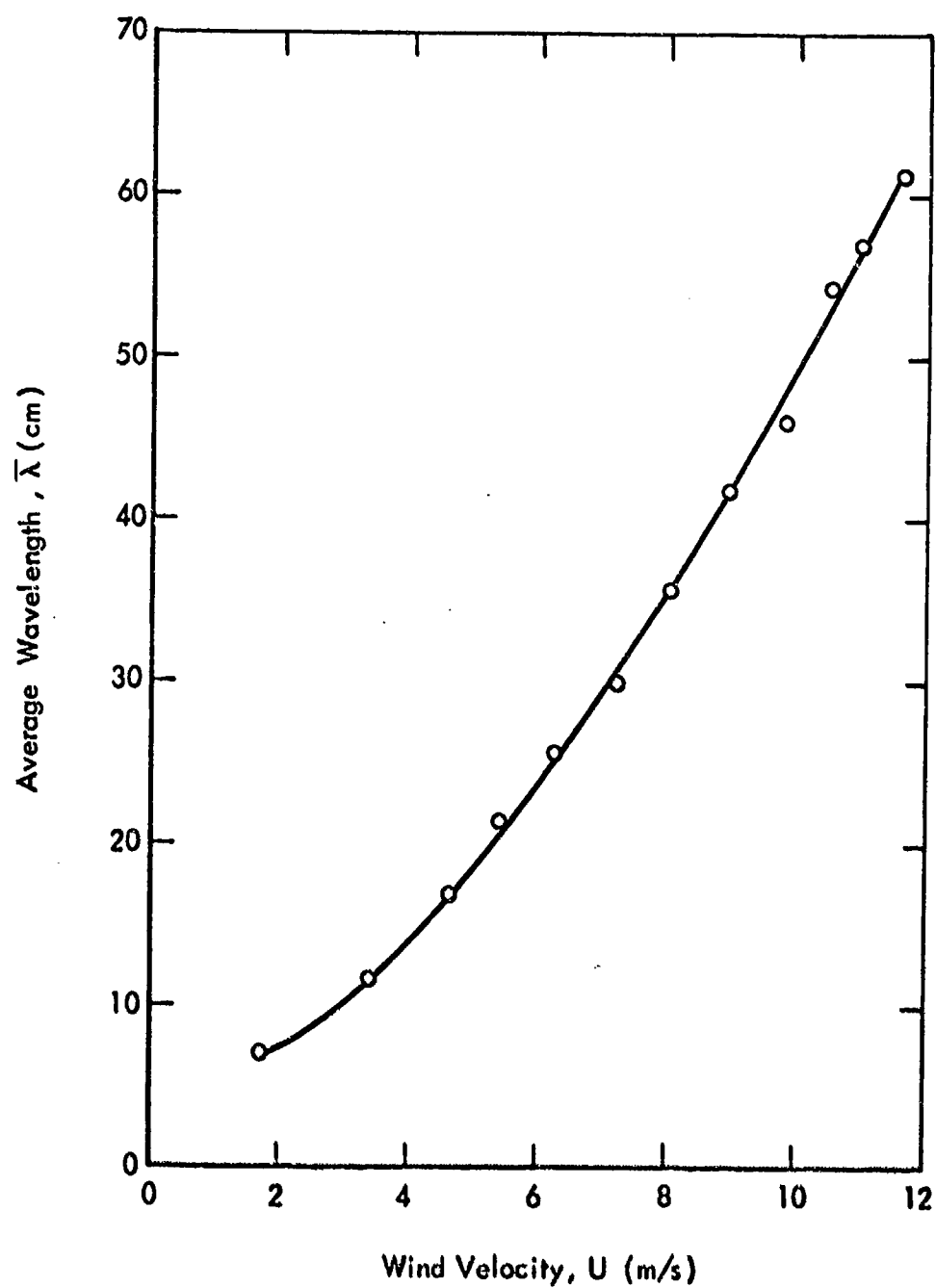
FIGURE 3 - AVERAGE WAVELENGTHS UNDER VARIOUS
WIND VELOCITIES
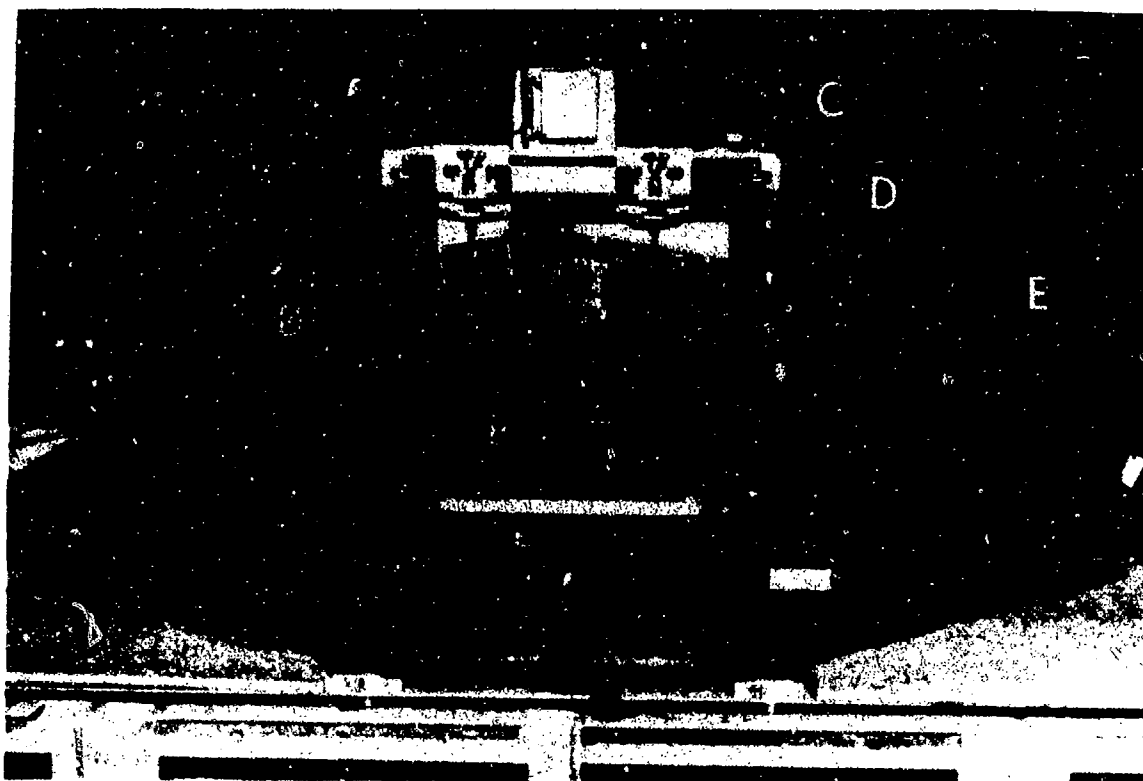
(a) Optical Instrument: A – Light source, B – Light receiver, C – Carriage, D – Vertical arch, E – Base ring

Angle of Inclination, θ (degrees)
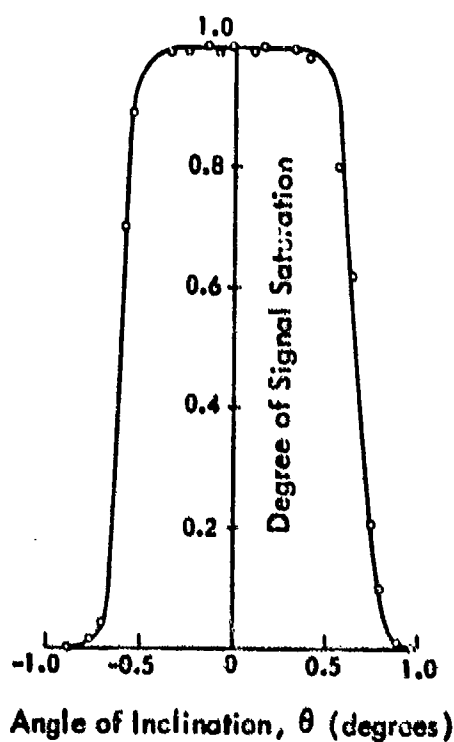
(b) Slope Response of Optical Instrument

Radius of Curvature, r (cm)
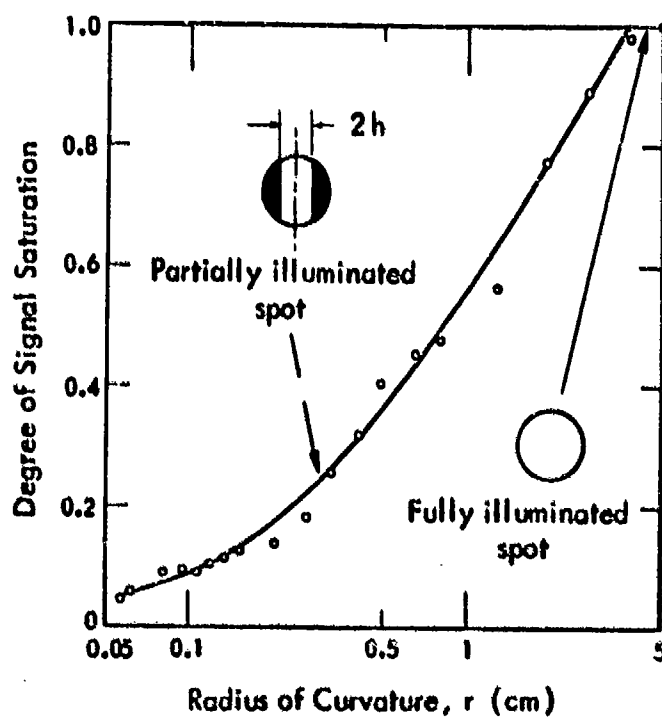
(c) Curvature Response of Optical Instrument

FIGURE 4 – OPTICAL INSTRUMENT AND ITS' SLOPE AND CURVATURE RESPONSES
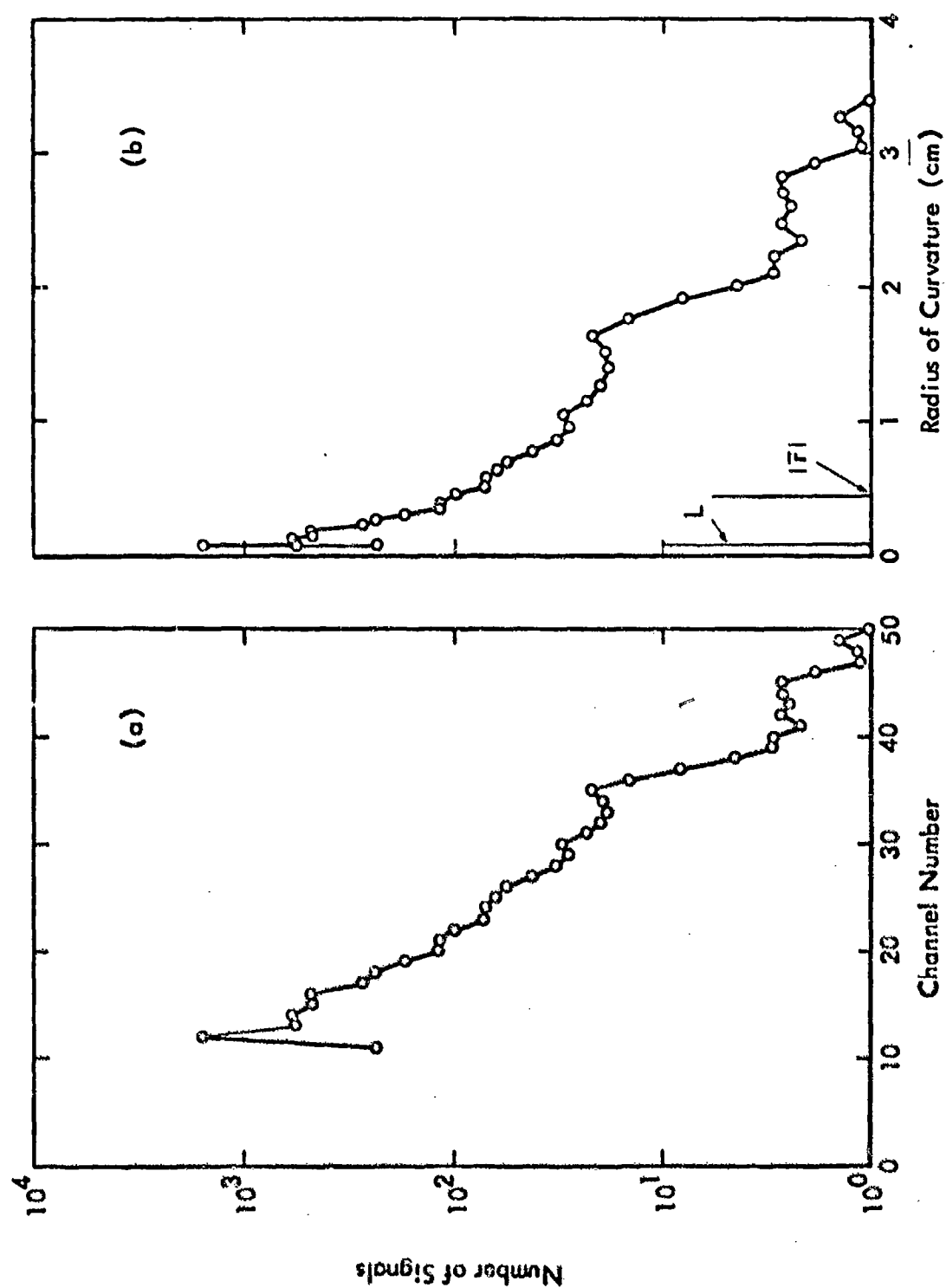
FIGURE 5 – TYPICAL DATA. In (b) L indicates the lower cutoff of the instrument and |r̄| is the average radius of curvature.
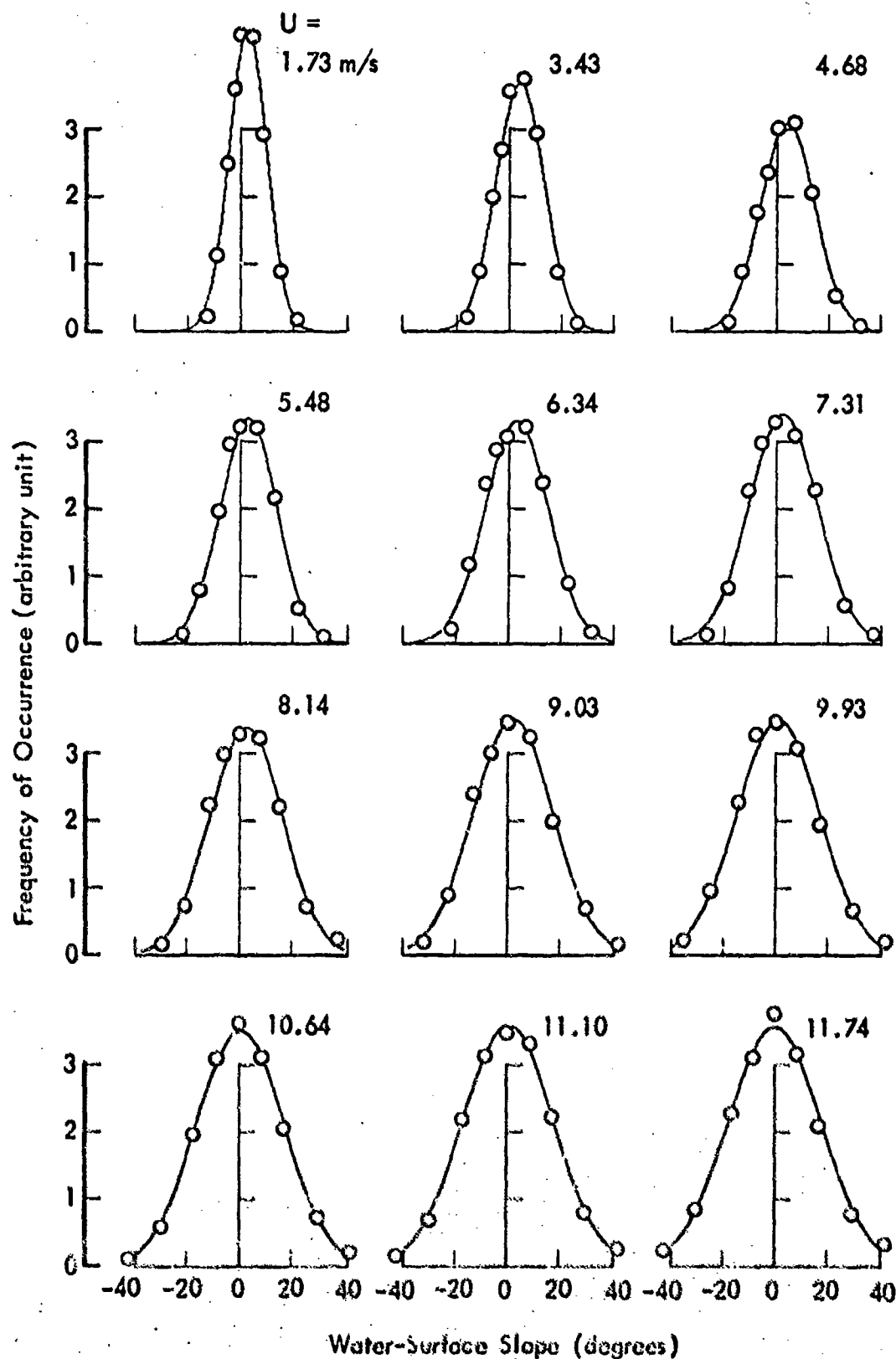
FIGURE 6 – DISTRIBUTIONS OF UPWIND-DOWNWIND SLOPES
UNDER VARIOUS WIND VELOCITIES

Water-Surface Slope (degrees)
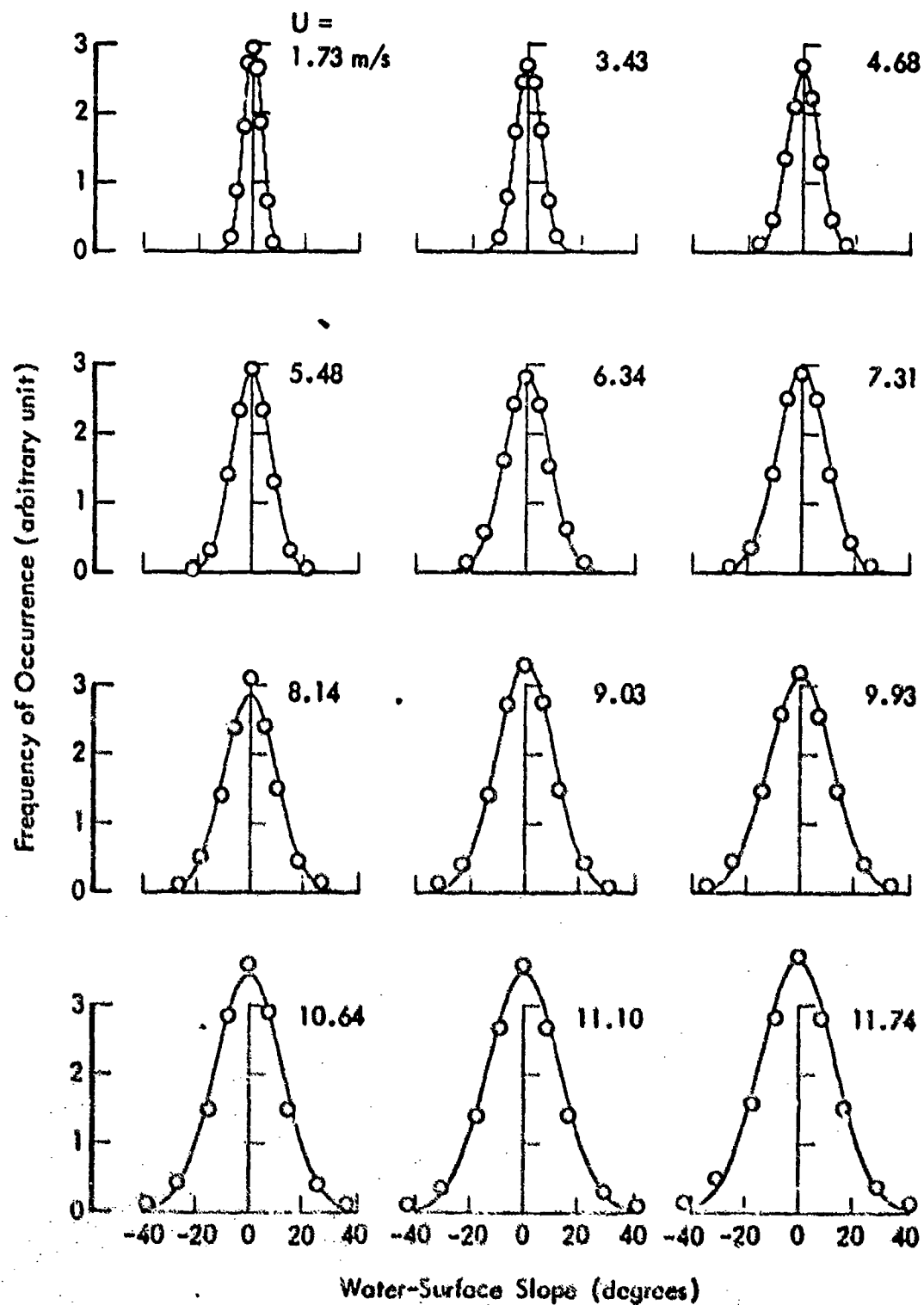
FIGURE 7 - DISTRIBUTIONS OF CROSSWIND SLOPES UNDER
VARIOUS WIND VELOCITIES
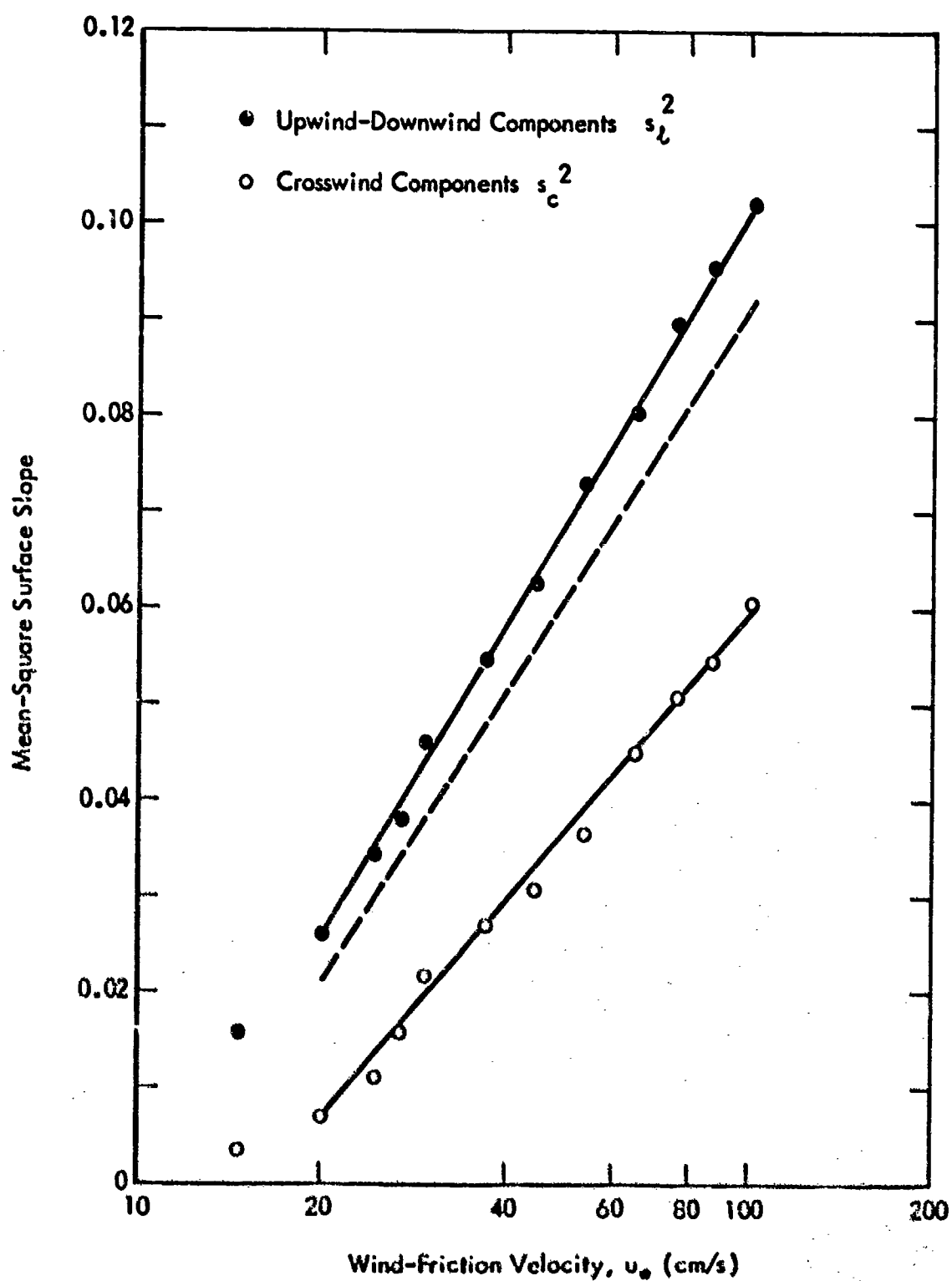
FIGURE 8 – MEAN-SQUARE UPWIND-DOWNWIND AND CROSSWIND
SLOPES UNDER VARIOUS WIND-FRICTION VELOCITIES.
The dashed line indicates previous measurements of upwind-
downwind slopes obtained at a shorter fetch.
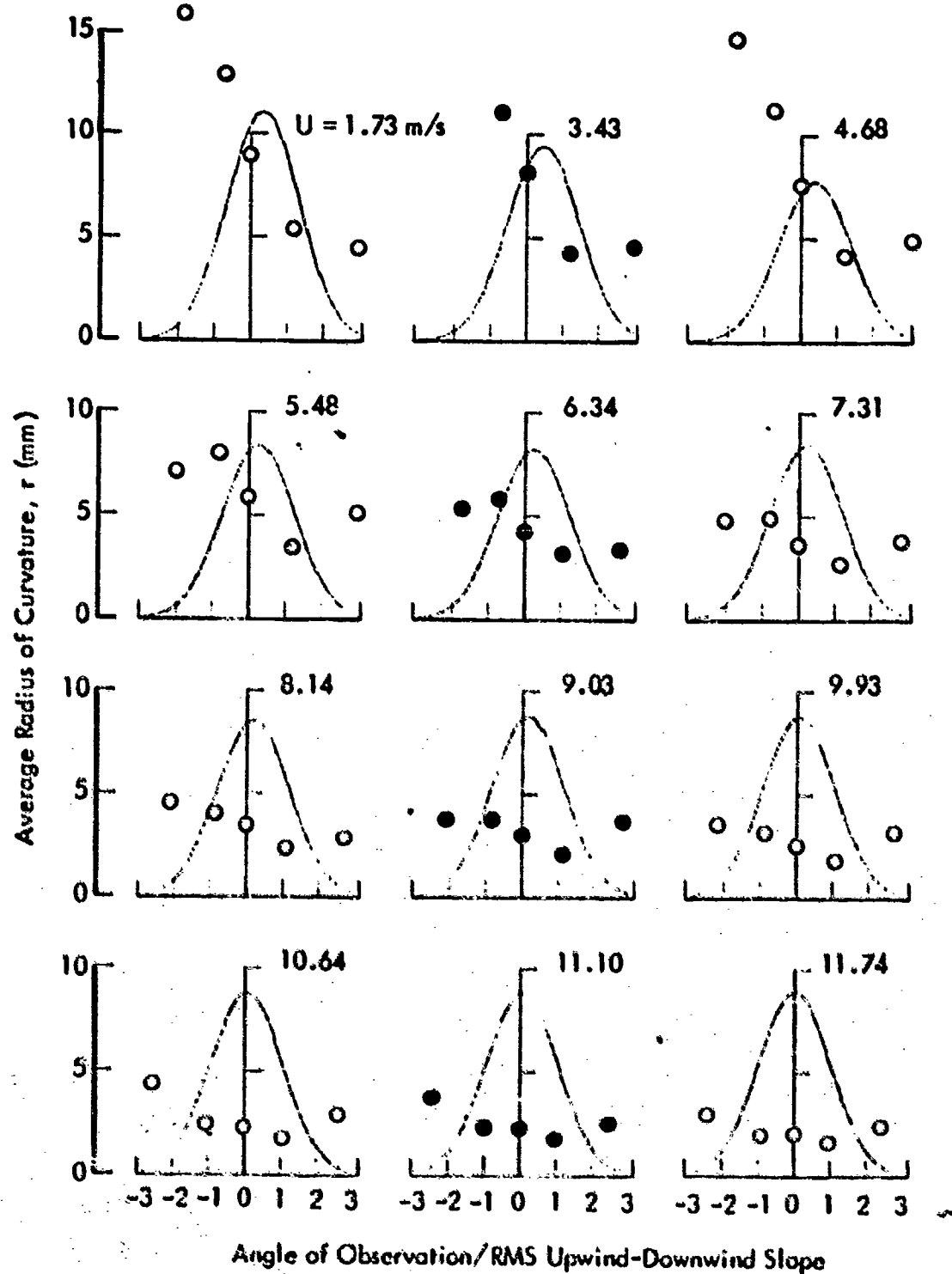
FIGURE 9 - RADII OF CURVATURE OF DISTURBED WATER SURFACES OBTAINED FROM VARIOUS ANGLES OF OBSERVATION ALONG UPWIND-DOWNWIND DIRECTION. The Gaussian curve indicates the frequency of occurrence of the upwind-downwind slope.
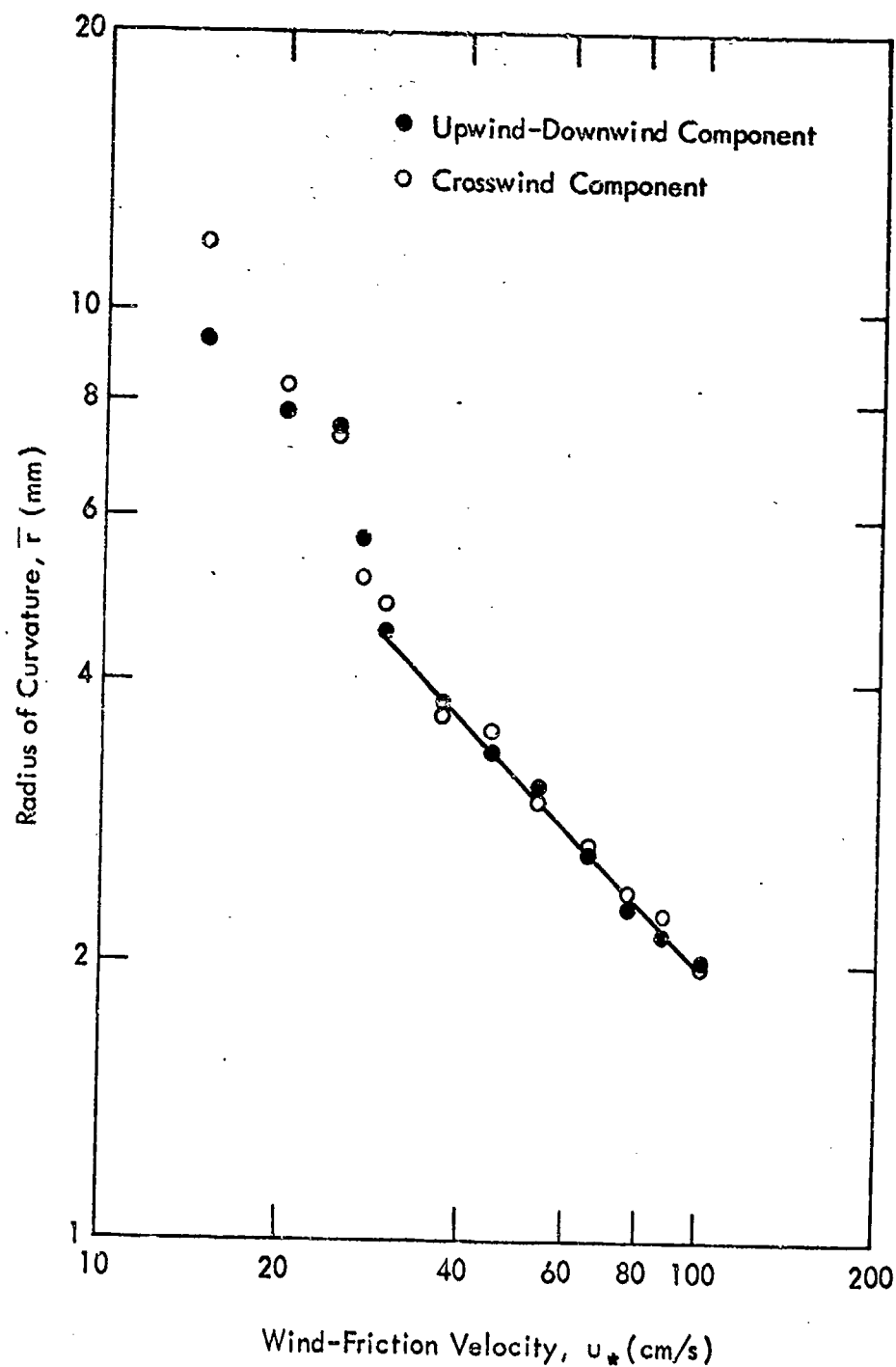
Angle of Observation/RMS Crosswind Slope
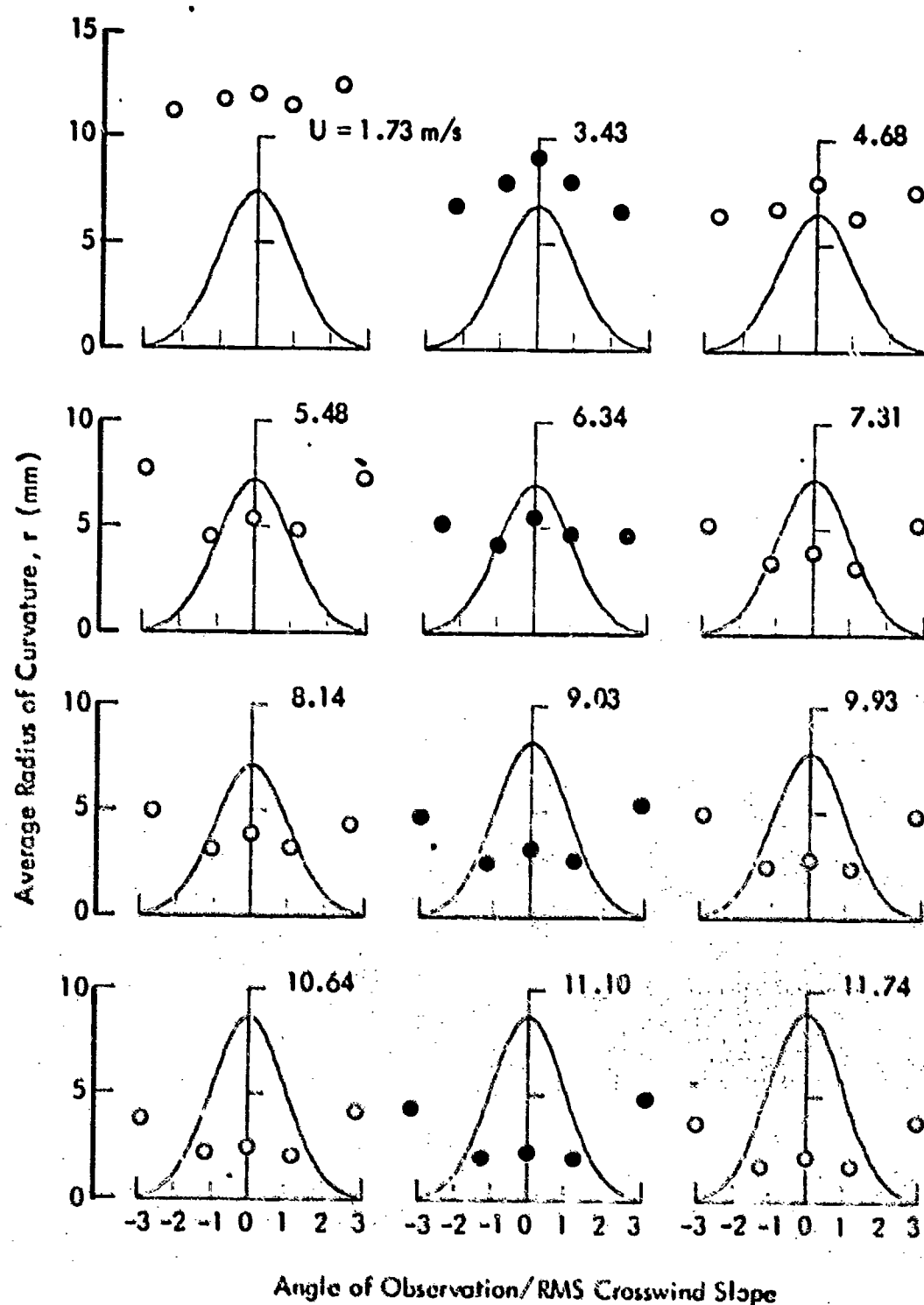
FIGURE 10 - RADII OF CURVATURE OF DISTURBED WATER SURFACES OBTAINED FROM VARIOUS ANGLES OF OBSERVATION ALONG CROSSWIND DIRECTION. The Gaussian curve indicates the frequency of occurrence of the crosswind slope.

FIGURE 11 - OVERALL AVERAGE RADII OF CURVATURE
OF WIND-DISTURBED SURFACES MEASURED
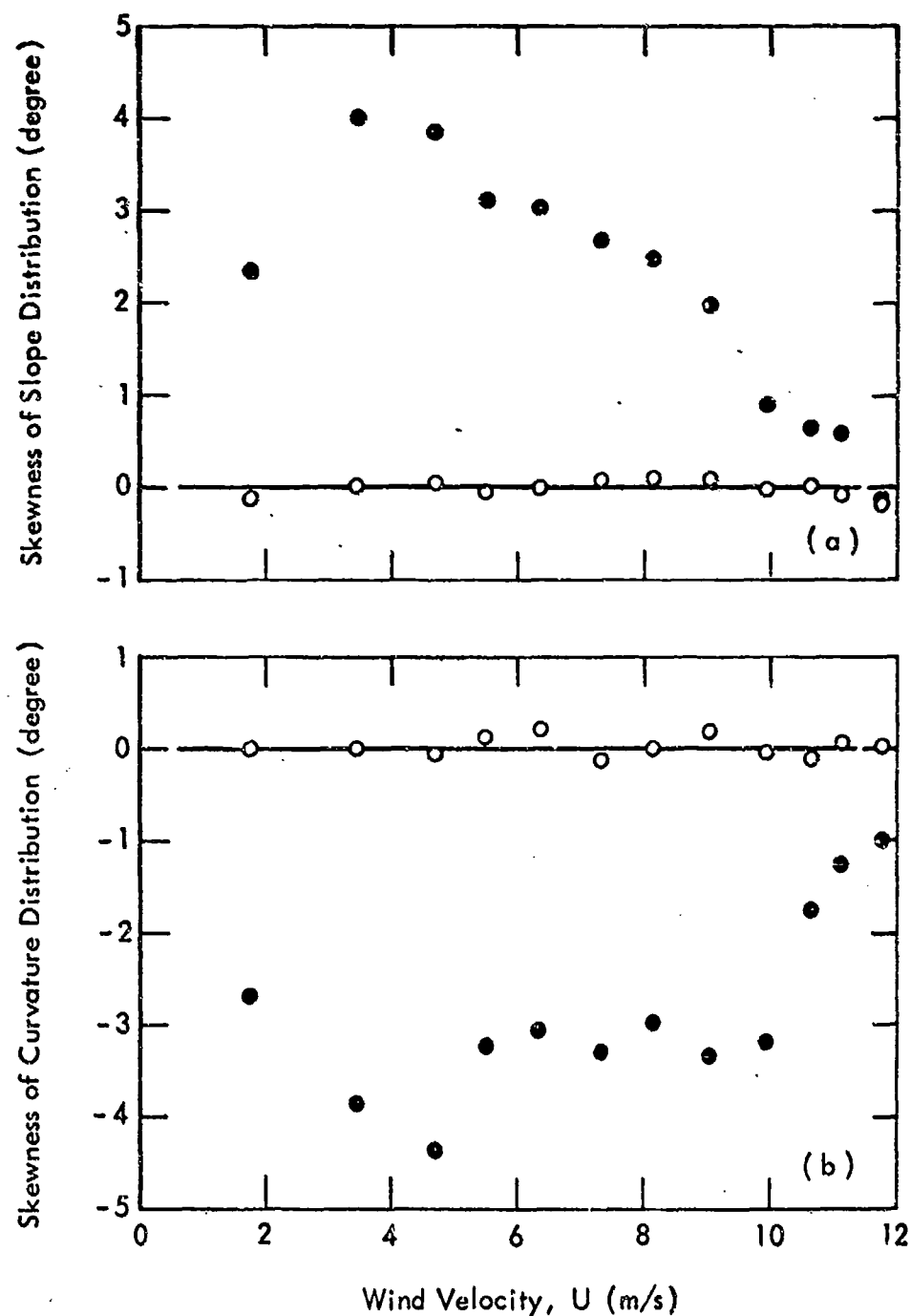ALONG UPWIND-DOWNWIND AND CROSS-
WIND DIRECTIONS

FIGURE 12 - SKEWNESS OF SLOPE AND CURVATURE
DISTRIBUTION MEASURED ALONG UP-
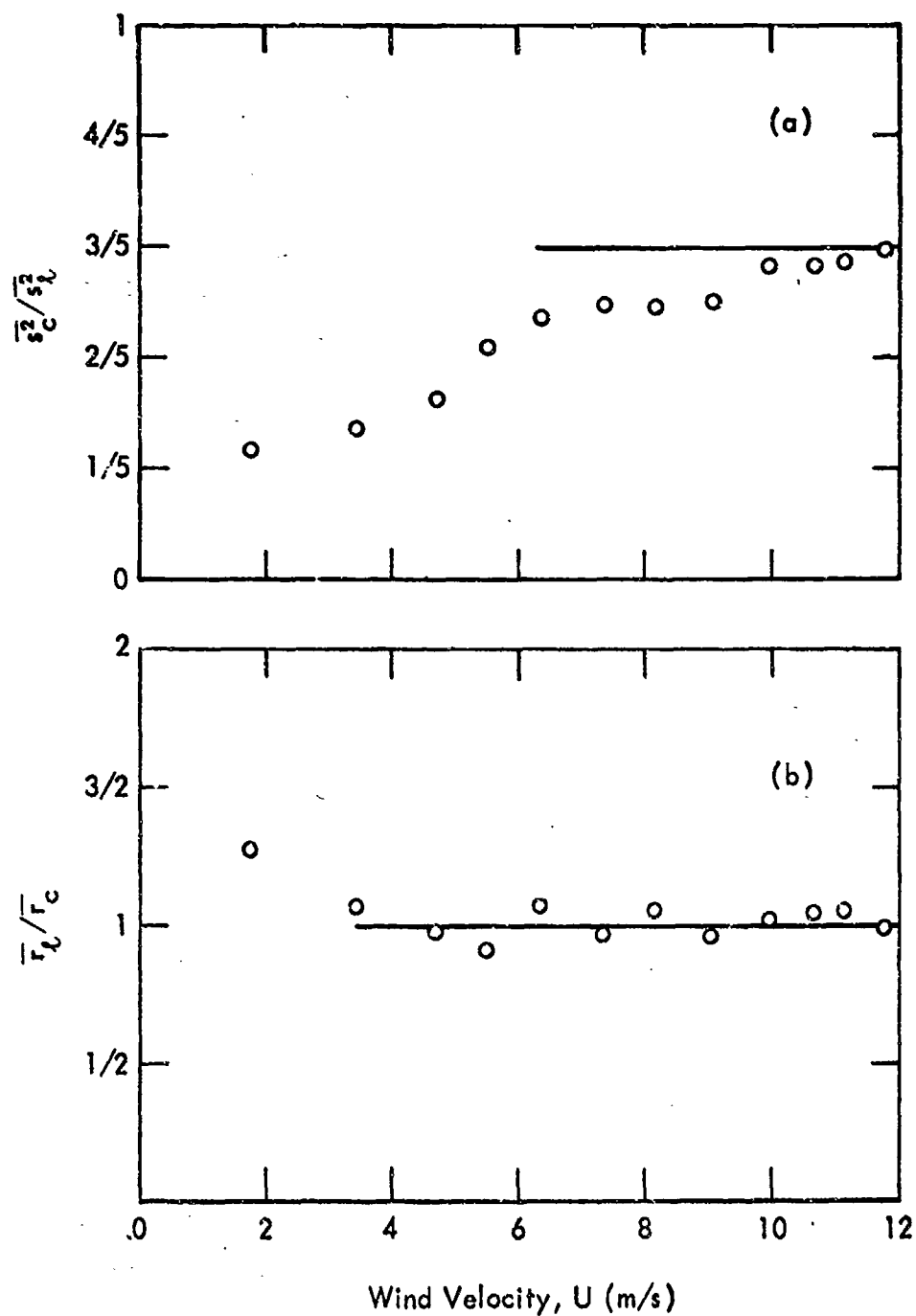WIND-DOWNWIND, ●, AND CROSS-
WIND, ○, DIRECTIONS

FIGURE 13 - RATIOS BETWEEN CROSSWIND AND UPWIND-
DOWNWIND COMPONENTS OF MEAN-SQUARE
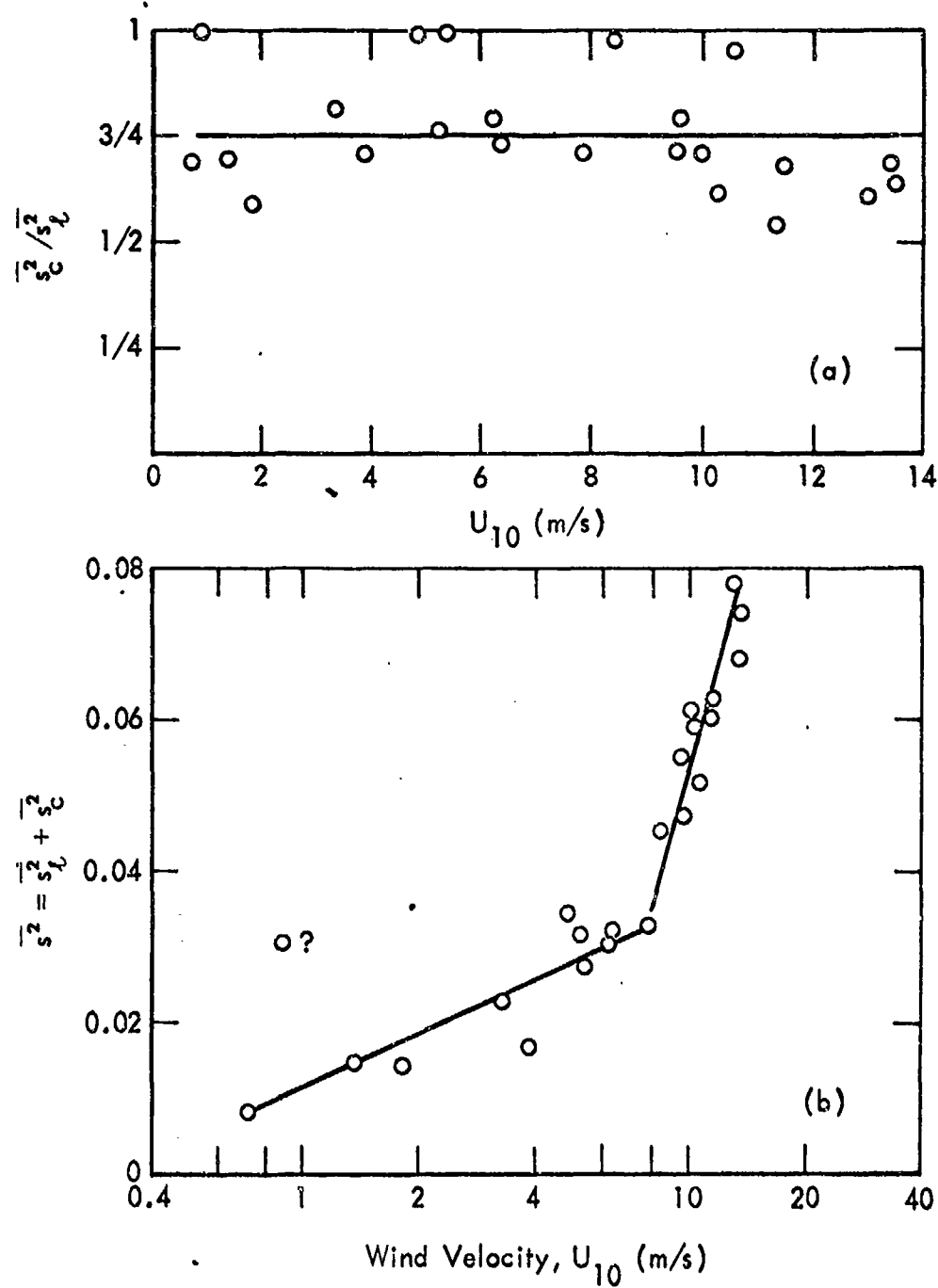SURFACE SLOPE (a) AND AVERAGE RADIUS OF
SURFACE CURVATURE (b)

FIGURE 14 - FEATURES OF OCEANIC SLOPE DATA. The
ratio between the crosswind and the upwind-
downwind mean-square slope is seen in (a) to
be about 3/4, and the total mean-square slopes
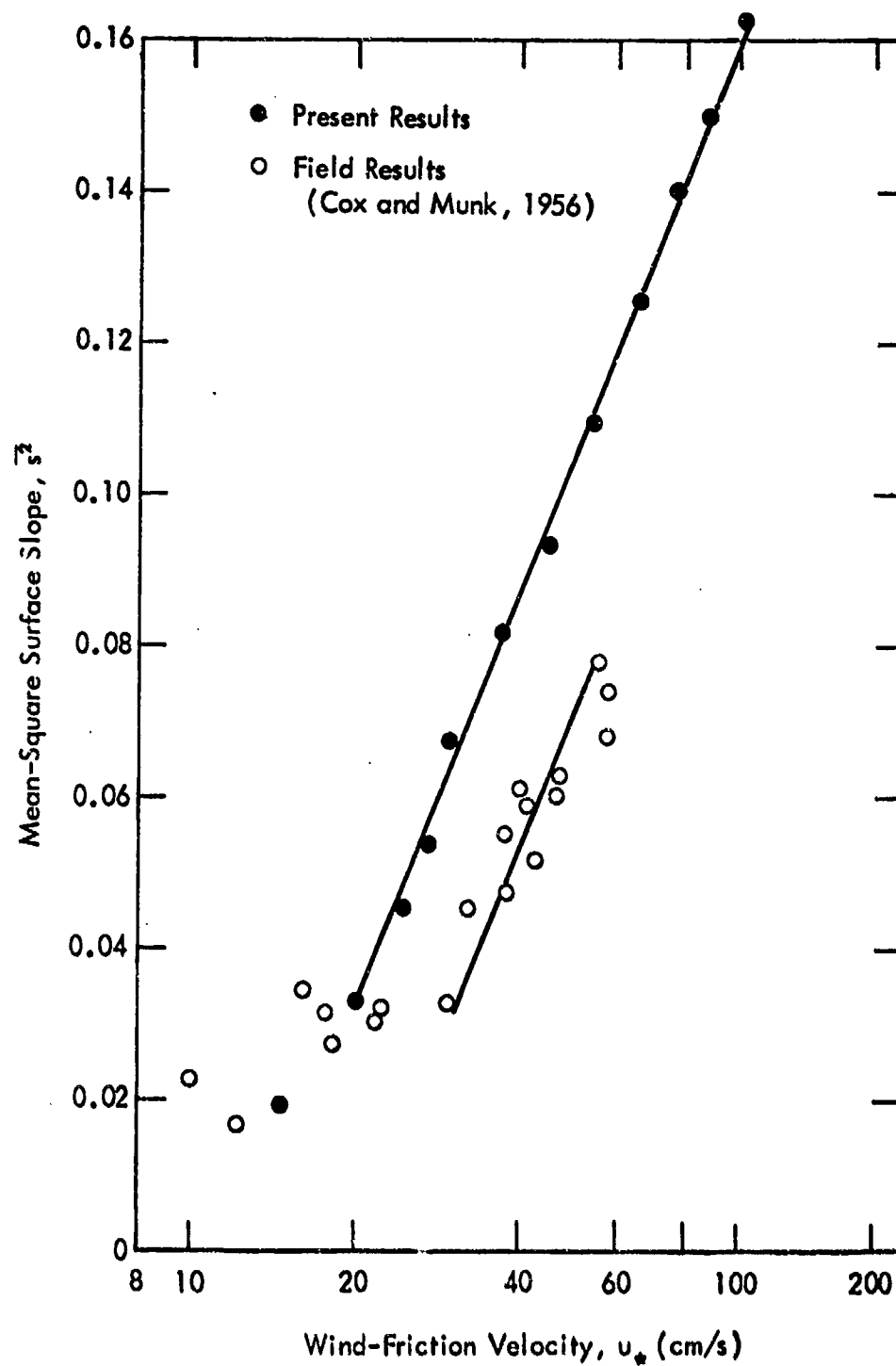are seen in (b) to be divided into two groups.

FIGURE 15 – COMPARISON OF LABORATORY AND FIELD
RESULTS OF MEAN-SQUARE SURFACE SLOPES